Check for updates

Synthesis and kinetic study of the photocatalytic efficiency of $Bi_{1-x}Dy_xFeO_3$ nanoparticles in the removal of Ponceau 4R dye

Elaheh Mahmoudi Doroh[1] · Razieh Sanavi Khoshnood[1] ⓘ **·
Davoud Sanavi Khoshnoud[2] · Zarrin Es′haghi[1,3]**

Abstract

In this study, a method for the removal of Ponceau 4R (P4R, E124) dye from aqueous solution using the chemical interaction of dye molecules with nano- $Bi_{1-x}Dy_xFeO_3$ is reported. $Bi_{1-x}Dy_xFeO_3$ (x = 0.00, 0.02, 0.04, 0.06) nanoparticles were synthesized using the sol–gel method. Structural, morphological, and optical properties of the nanoparticles were X-ray diffraction analysis (XRD), field emission-scanning electron microscopy (FE-SEM), and ultraviolet–visible (UV–Vis) spectroscopy at room temperature. The photocatalytic degradation of P4R was optimized under these conditions: The P4R concentration of 20 mg L^{-1} of P4R, 0.50 mL hydrogen peroxide (H_2O_2), 0.10 g of the catalyst, and under the influence of an ultraviolet lamp at pH 2. The photocatalytic result indicates that Dy-doped $BiFeO_3$ (BFO) nanoparticles improved photocatalytic activities compared with BFO. Under optimum conditions, the percentages of P4R degradation using BFO for 240 min was 98.92%, using BFO Dy-doped (Dy 2%), (Dy 4%) and (Dy 6%) for 90 min 94.67%, 87.69%, and 79.69%. Also, the photodegradation kinetics of P4R in the presence of $Bi_{1-x}Dy_xFeO_3$ nanoparticles were investigated using the Langmuir–Hinshelwood model by determining the pseudo-first-order rate constant for the photodegradation. The results showed photodegradation rate constants (k) for a period of 90 min in the presence of the $Bi_{1-x}Dy_xFeO_3$ were 0.01031, 0.02312, 0.01830, and 0.01346 Cm^{-1} for x = 0.00, 0.02, 0.04, and 0.06.

Keywords Photocatalyst activity · Nanoparticles · Sol–Gel · P4R degradation

Introduction

Environmental pollution has increased in recent years due to the production of many pollutants such as organic dyes in various industrial sectors, such as paper, leather, fertilizer, food, cosmetics, pharmaceuticals, and textile industries, which

---

is an important source of specified environmental pollution [1]. Organic dyes have become an important part of industrial wastewater due to their extensive application and large-scale production [2]. Wastewater must be treated before reuse is possible [3]. Photocatalytic water purification is used due to its advantages such as excellent performance, performance at ambient pressure and temperature, low cost, and non-production of secondary waste, which makes it safe for the environment [4].

Materials with special nanostructures have attracted a lot of attention in the field of materials science due to their unique physical and chemical properties, which are distinctly different from normal materials, among which bismuth ferrite nanoparticles can be mentioned [5, 6]. BFO is regarded as a potential visible-light photocatalyst for the degradation of organic pollutants, due to its high photosensitivity at narrow band gaps with high excitation binding energy, non-toxicity, chemical stability, low cost, and multiferroic properties at room temperature [7, 8]. Since BFO possesses a narrow band gap energy, it is responsive to a wide spectrum of solar or visible light [9–16]. Besides, its multiferroic behavior is a contributing factor to the recyclability of a photocatalyst [17]. The investigation of the origin of magnetism in BFO could reveal interesting insights into its magnetic phenomena [18]. BFO exhibits enhanced magnetic properties through the suppression of its cycloidal AFM spin structures and the formation of AFM/FM core/shell structures [19, 20]. The magnetic property that occurs due to one of these origins would also influence other properties of BFO. On the other hand, BFO also exhibits visible-light-driven photocatalytic activity that is currently being explored for applications such as water splitting for hydrogen production and degradation of organic pollutants [21, 22]. The rare earth element dysprosium (Dy) is chosen as a substituent because it could enhance the magnetic property by suppressing the cycloidal spin structure in the host BFO [23]. Furthermore, its optical properties and 4f shell electronic configuration is expected to enhance visible light absorption and photocatalytic properties [24].Various methods including the sol–gel method, hydrothermal methods, solid state reaction, co-precipitation synthesis, rapid liquid-phase sintering method, pulsed laser deposition, electro-spinning and magnetron sputtering have been utilized to obtain BFO nanoparticles with determined sizes. Among these techniques, the sol–gel synthesis method is widely used for the synthesis of BFO, because it allows obtaining pure phases and controlling the size and distribution of particles. Also, by comparing the sol–gel method with other BFO synthesis techniques, we see that the sol–gel method is often considered a superior choice due to the many advantages it offers including the ability to produce nanostructured materials with high purity and good homogeneity, as well as the ability to control the size and shape of the resulting particles. The sol–gel method also allows the incorporation of impurities and other additives that can significantly change its physical and chemical properties [25, 26]. P4R is poisonous and carcinogenic aromatic ring structures and azo functional groups (–N=N–) [27]. Therefore, P4R is likely to lead to many adverse health effects such as allergies, neurobehavioral toxicities, and cancers if it is excessively consumed. The molecular structure of P4R is shown in Fig. S1. [28]. To guarantee food safety, the dosages of P4R have been severely restricted by laws and regulations. For example, the joint FAO/WHO Expert Committee on Food

Additives (JECFA) has set the acceptable daily intake (ADI) for P4R as 4.0 and mg/kg bw/day [29].

The main purpose and advantage of this study is the photocatalytic degradation of P4R dye in the presence of BFO nanoparticles synthesized by the sol–gel method to find other means to speed up the efficiency of the photocatalytic process and remove pollutants from the environment. Therefore, the effect of different parameters such as the type of light irradiation, the amount of H_2O_2, the amount of pH and the amount of catalyst including BFO nanoparticles and BFO doped with dysprosium were also investigated to optimize the process for maximum degradation of P4R using UV–Vis spectroscopy. Among the optimal cases, the doping of BFO with rare earth metals through the creation of electron–hole trapping centers in the photocatalyst network has a great effect on the efficiency of the photocatalytic process, which is a vital method to improve the photocatalytic properties of semiconductors. Introducing doping by rare earth metals can improve the photocatalytic efficiency of BFO by reducing the particle size and increasing its surface area. In the continuation of this study, the optical properties and photocatalytic activity of pure BFO nanoparticles and BFO doped with dysprosium were investigated.

Experimental

Materials

The materials used:

- Bismuth nitrate pentahydrate [Bi $(NO_3)_3 \cdot 5H_2O$] and dysprosium nitrate pentahydrate [Dy $(NO_3)_3$ $5H_2O$] from Chem-Lab NV (Belgium),
- Iron nitrate nonahydrate [Fe $(NO_3)_3 \cdot 9H_2O$] from Scharlab S.L. (Spain),
- Tartaric acid ($C_4H_6O_6$) from LOBA CHEMIE PVT. LTD. (India) and Ponceau 4R ($C_{20}H_{11}N_2Na_3O_{10}S_3$) from Merck (Germany).

Ammonia (NH_3), hydrochloric acid (HCl), sodium hydroxide (NaOH), nitric acid (HNO_3), and hydrogen peroxide (H_2O_2) were purchased from Merck too. Aqueous solutions were used with double distilled water.

Instruments

A UV–Vis spectrophotometer (Varian Cary 50 Bio, Australia) was used to measure the absorbance of P4R dye. The XRD pattern was performed using an X-ray diffractometer (Bruker D8 ADVANCE, Germany). Morphology and the particle size of BFO and Dy-doped BFO nanoparticles were used by field-emission scanning electron microscopy (FE-SEM, TESCAN MIRA3, Czech Republic). The local structure of the nanoparticles was obtained with Fourier-transform infrared spectroscopy (FT-IR, Bruker Optik GmbH TENSOR 27, Germany). The optical properties were calculated with the help of diffuse reflectance spectra (DRS, PerkinElmer, LAMBDA

365 UV–Vis spectrophotometer, United States). From oven (Pars Azma Co K.J 55, Iran) and an electric muffle furnace (SCI FINETECH FTMF706/706P, Korea) were utilized in the synthesis of BFO and Dy-doped BFO. A mercury vapor lamp (250 W) was utilized for the photocatalytic activity of BFO and $Bi_{1-x}Dy_xFeO_3$ (x = 0.02, 0.04, and 0.06) nanoparticles for the P4R removal. The pH measurements were used using a pH meter (Metrohm 780, Switzerland), and stirring of the solution was performed with a magnetic stirrer (Heidolph Hei-Standard, Germany).

Synthesis of BFO and Dy-doped BFO nanoparticles

The typical sol–gel method was used to synthesis of BFO and $Bi_{1-x}Dy_xFeO_3$, x = 0.02, 0.04, and 0.06 nanoparticles and photocatalyst was prepared with the tartaric acid assisted. In this method, an appropriate amount of $Bi(NO_3)_3 \cdot 5H_2O$, $Fe(NO_3)_3 \cdot 9H_2O$, and $Dy(NO_3)_3 \cdot 5H_2O$ were added into a solution containing 1 mL of HNO_3 and 20 mL of distilled water [30, 31]. The mixture was stirred for 1 h at 60 °C and 750 rpm to completely dissolve all materials, after the addition of tartaric acid and ethylene glycol. Following, the mixture was stirred at room temperature for 2 h and a lemon-color suspension was found. The suspension was continuously stirred, and NH_3 1 mol L^{-1} was added dropwise to the suspension to adjust the pH. The XRD results showed that the best BFO and Dy-doped BFO nanoparticles were obtained at pH 6. The suspension was heated with a thermal program up to 200 °C in the oven. The obtained powder was calcined in a furnace for 3 h with a thermal program to 400 °C. For removal impurities in of phases such as $Bi_2Fe_4O_9$ and $Bi_{25}FeO_{39}$, the powder was filtered and washed several times with HNO_3 0.10 mol L^{-1} and deionized water. In the end, the powder for the second time, was heated in a furnace at 650 °C for 4 h.

Photocatalytic experiment

The photocatalytic activity of the BFO and Dy-doped BFO nanoparticles were evaluated in the aqueous solution of P4R under different conditions of darkness, sunlight, and UV light irradiation. At first, calibration steps were performed to determine the P4R initial concentration that acquired 20 mg L^{-1}. Then 300 mL of P4R dye with a concentration of 20 mg L^{-1} was prepared and transferred to a 600 mL beaker. Next, H_2O_2 and the nano catalysts were added into the beaker comprising 300 mL P4R solution. The pH of P4R aqueous solutions was adjusted at different amounts using HCl and NaOH 1 mol L^{-1}. Then, the beaker was placed inside the photoreactor and the solution was stirred at 750 rpm. The lamp was turned on and every 15 min, 3 mL of the sample was pipette for 240 min.

This handmade reactor was composed of a UV lamp, two fans, and a magnetic stirrer. The distance between the lamp and the starter was 18 cm. The handmade reactor had dimensions of 50 cm width × 75 cm length × 40 cm height and two places on top of the reactor for sampling. In the following, the degradation of P4R dye was investigated by measuring the absorption of the P4R dye aqueous solution

at $\lambda_{max} = 508$ nm using a UV–Vis spectrophotometer. The degradation efficiency of the P4R dye was determined by the following equation (Eq. 1) [32]:

$$\text{Degradation efficiency} (\%) = (C_0 - C_t)/C_0 \times 100 \tag{1}$$

In the above formula, C_0 and C_t are P4R concentrations (mg L^{-1}) at the initial concentration of the dye (t = 0 min) and at irradiation times (t = 0–240 min).

Results and discussions

Characterization of nanomaterials

Nano photocatalyst powders were characterized by means of X-ray diffraction (XRD), FE-SEM analysis, Fourier transform infrared spectroscopy (FTIR), as well as their optical properties.

XRD analysis

The X-ray diffraction (XRD) pattern of $Bi_{1-x}Dy_xFeO_3$ nanoparticles (NPs) is shown in Fig. 1a. To investigate the purity of $Bi_{1-x}Dy_xFeO_3$ NPs and estimate possible impurity phases, X'pert software was used. Investigations indicate that $Bi_{1-x}Dy_xFeO_3$ NPs are almost single-phase. However, a small number of impurity phases, including $Bi_2Fe_4O_9$ and Bi_2O_3 existed as indicated in Fig. 1a with symbols (+) and (*). With substituting Dy ion at the Bi site two phenomena including merging doublet peaks and shifting peaks occur in XRD patterns as shown in Fig. 1a. Both phenomena are due to the difference in ion radii of Bi and Dy.

It is known that BFO crystalizes in a rhombohedral structure with the R3c space group. To determine the space group of other samples and structural parameters, the Fullproof software was used. For instance, Fig. 1b indicates the Rietveld refinement for $Bi_{1-x}Dy_xFeO_3$ NPs. Moreover, the lattice constants (a, b, and c) and unit cell volume (V) of $Bi_{1-x}Dy_xFeO_3$ NPs were calculated and listed in Table 1. The results show that V decreases with increasing Dy content. This Result always occurs in BFO by replacing rare earth ions (Dy) for the Bi site corresponding to the difference between ion radii of Bi and Dy [33–36].

FE-SEM analysis

The FE-SEM images of $Bi_{1-x}Dy_xFeO_3$ NPs are shown in Fig. S2. By comparing images can be concluded that with increasing Dy substitution the particles are more homogenous. The insets exhibit the size particle distribution histogram of $Bi_{1-x}Dy_xFeO_3$ NPs. The mean particle diameter (D_{SEM}) of $Bi_{1-x}Dy_xFeO_3$ NPs was calculated using the log–normal function [37–39]. The D_{SEM} of our samples were listed in Table 1.
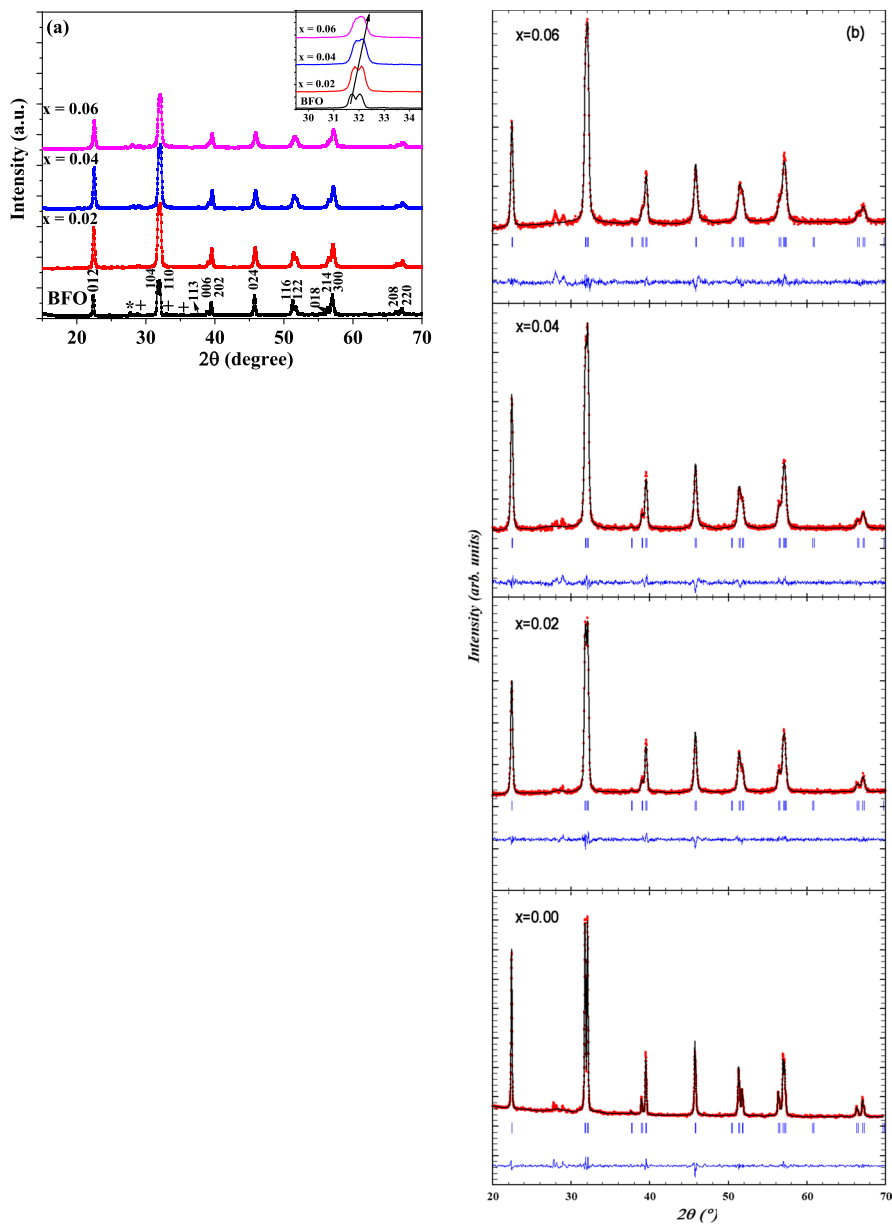
Fig. 1 **a** XRD pattern of $Bi_{1-x}Dy_xFeO_3$ nanoparticles, inset: merging and shifting in doublet major peak, and **b** the Rietveld refinement for $Bi_{1-x}Dy_xFeO_3$ NPs

To study the elemental composition of $Bi_{1-x}Dy_xFeO_3$ NPs, energy dispersive spectroscopy (EDS) characterization was used. The existence of all elemental stoichiometric composition is confirmed as shown in Fig. S3 that the synthesized sample contains the expected amounts of Bi, Fe, Dy, and O.

Table 1 The lattice parameters (a, b, and c), unit cell volume (V), mean particle diameter (D_{SEM}) and energy gaps of $Bi_{1-x}Dy_xFeO_3$ nanoparticles

Sample	a = b (Å)	c (Å)	V (Å)3	DSEM (nm)	Energy gap (eV)
x = 0.00	5.577(2)	13.866(1)	373.50(2)	108	2.17
x = 0.02	5.575(4)	13.855(0)	372.98(8)	72	2.18
x = 0.04	5.574(2)	13.846(5)	372.59(1)	66	2.21
x = 0.06	5.573(7)	13.835(3)	372.13(5)	68	2.20

FT-IR spectrum

In Fig. S4, the FTIR spectra, which corresponded to the samples prepared in the presence of dysprosium, were recorded within the range of 400–4000 cm^{-1}. The FT-IR spectrum shows that the characteristics peak in the range of 400–600 cm^{-1} which can be ascribed to the Fe–O stretching and bending vibrations [40, 41]. These vibrational states are specifications of the octahedral FeO_6 groups on the perovskite structure which imply the formation of BFO [42]. The broad bands that are positioned in the range of 3400 and 1630 cm^{-1} correspond to the ν(O–H) stretching and δ(O–H) bending vibrations of the hydroxyl groups [43, 44].

Optical properties

To study the band gap energy of $Bi_{1-x}Dy_xFeO_3$ NPs used DRS analysis. Using the Kubelka–Munk (K–M) formula, $F(R) = (1 - R)^2/2R$, where R is the reflectance of the $Bi_{1-x}Dy_xFeO_3$ NPs [45]. Then, to determine the E_g of $Bi_{1-x}Dy_xFeO_3$ NPs, the curve of $(F(R) \times h\nu)^2$ versus $h\nu$ was plotted. For instance, the curve of E_g for $Bi_{1-x}Dy_xFeO_3$ NPs were shown in Fig. 2. The E_g value for $Bi_{1-x}Dy_xFeO_3$ NPs were given in Table 1. It is clear that the band gap energy changes negligibly with Dy content. In general, the band gap of a compound can be depending on particle size, shape, and porosity and crystal distortion [15, 36, 46, 47]. In BFO with low doping levels noticeable changes in band gap do not observe corresponding to above mentioned factors. This behavior agrees with the literature [48, 49].

Photodegradation of P4R dye

The photocatalytic activity of pure BFO and Dy-doped BFO nanoparticles was investigated to degrade P4R dye under a dark state, sunlight, and UV light irradiation. It can be seen that the BFO nanoparticles produced by doping Dy show higher photocatalytic activity under UV-light irradiation [50]. In the following, to increase the efficiency of photocatalytic activity, the effect of various operation parameters, such as BFO dosage, initial PH of the dye, presence, and dosage of H_2O_2, and type of light irradiation, was studied and optimized as a function of time.
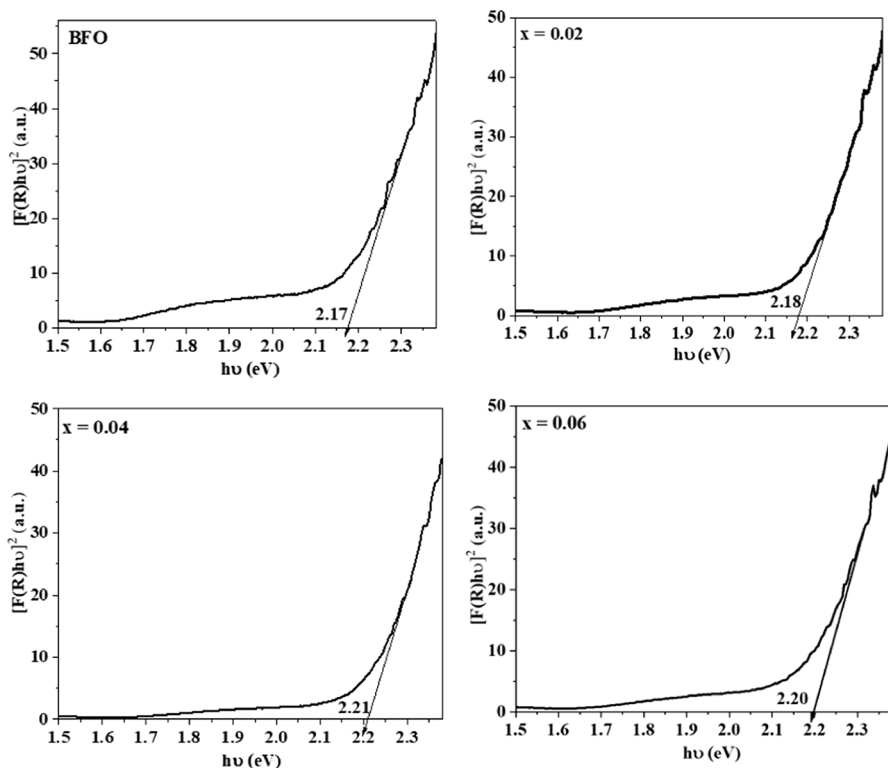
Fig. 2 $(F(R) \times h\upsilon)^2$ versus photon energy ($h\upsilon$) for $Bi_{1-x}Dy_xFeO_3$

Effect of irradiation type on the removal efficiency of P4R dye

The photocatalytic activity of BFO nanoparticles was measured in three modes: dark, direct sunlight, and direct UV light. In the dark state, it has the least amount of degradation, then in the direct sunlight mode, and most of the degrading is in the UV light radiation mode, Fig. 3. UV light helps to produce more hydroxyl radicals (OH·), but sunlight has only 3 to 4% of ultraviolet rays and the amount of degradation is much less than UV light [51].

Effect of H_2O_2

Apart from its photocatalytic property, BFO also exhibits prominent photo -Fenton-like catalysis ability. The degradation of P4R is carried out in the absence and presence of H_2O_2 with different amounts including (0.25, 0.50, 0.75, and 1 mL) at pH 2 under UV light irradiation for 240 min. It can be seen from Fig. 4a. That the best value of H_2O_2 was 0.50 mL. The percentage of degradation of P4R in the presence of 0.50 mL H_2O_2 was slightly increased compared to other quantities, and
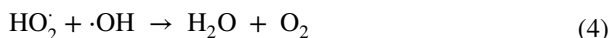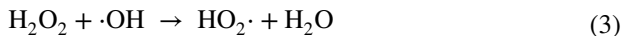
Fig. 3 The percentage of degradation of P4R in a dark state, sunlight, and UV light irradiations. Experimental conditions: concentration of 20 mg L^{-1} of P4R, 0.50 mL H$_2$O$_2$, 0.10 g of the pure BFO nanoparticles and pH 2 nanoparticles and pH 2
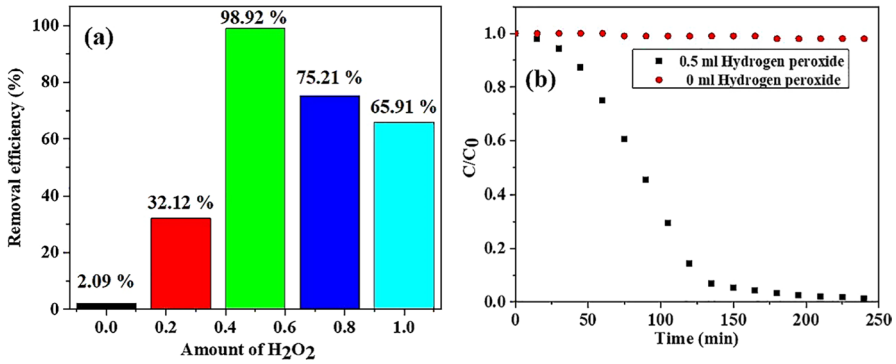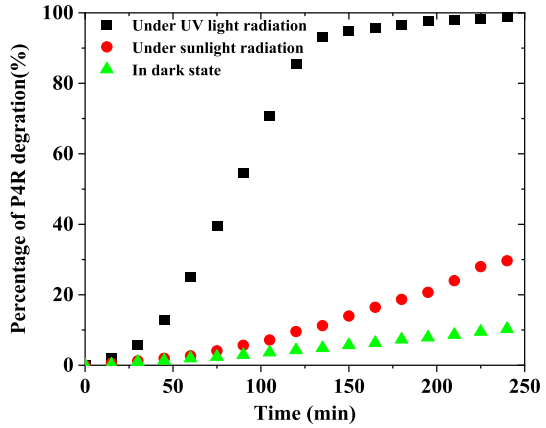
Fig. 4 **a** The rate of percentage of degradation of P4R at different H$_2$O$_2$ values (0, 0.25, 0.50, 0.75, and 1 mL) and **b** The photocatalytic degradation process of P4R in the absence and presence of H$_2$O$_2$. Experimental conditions: concentration of 20 mg L^{-1} of P4R, 0.10 g of the pure BFO nanoparticles, under UV light irradiation and pH 2

the absence and presence of 0.50 mL H$_2$O$_2$ were 2.09% and 98.92% Fig. 4b. Compared with the reaction systems without H$_2$O$_2$, the introduction of H$_2$O$_2$ remarkably enhances the degradation percentage of the dye. This result is mainly due to the photo -Fenton-like reaction mechanism. The H$_2$O$_2$ is an electron scavenger that can produce ˙OH radicals. Therefore, it increases the separation of the hole and the electron, which enhances the degradation efficiency [52]. With the addition of 0.50 mL of H$_2$O$_2$, the photocatalytic activity for the degradation of P4R dye increases due to the higher generation of ˙OH radicals and dye adsorption on the surface of BFO nanoparticles (Eq. 2). At the highest amount of H$_2$O$_2$, it decreased the rate of the dye reaction due to competition with P4R for the available ˙OH radicals (Eqs. 3 and 4) [53].

$$H_2O_2 + BFO(e^-) \rightarrow \cdot OH + OH^- + BFO \tag{2}$$

$$H_2O_2 + \cdot OH \; \rightarrow \; HO_2 \cdot + H_2O \tag{3}$$

$$HO_2^{\cdot} + \cdot OH \; \rightarrow \; H_2O \; + \; O_2 \tag{4}$$

Effect of the BFO nanoparticles dosage

Catalyst and H_2O_2 together affect degradation and are not important factors in degradation separately. To optimize the amount of the nanoparticles, different dosages (0, 0.05, 0.10, 0.15, and 0.20 g) were tested Fig. 5. The presence of a catalyst is significant and influential in the rate of P4R degradation. In the absence of BFO, the amount of photocatalytic degradation was very negligible. It was found that 0.10 g of BFO is the optimum dosage for the degradation of P4R. With the increase of catalyst dosage to 0.10 g, the availability of more active sites on the catalyst surface increases. In the amounts of 0.15 and 0.20 g of catalyst, particle aggregation reduces the photocatalytic degradation activity by reducing the specific surface area probability [54–56]. When the catalyst and H_2O_2 are added, the degradation efficiency in the dye solution increases to 98.92% within 240 min. Therefore, we conclude that the photo -Fenton process plays a significant role in the production of ·OH radicals.
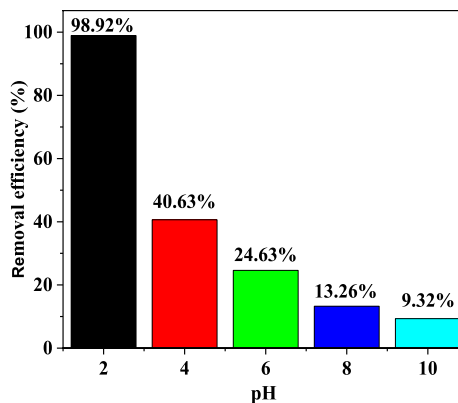
Investigation of initial pH of P4R

pH is one of the main parameters, the effect of which usually goes back to the existing functional groups on the catalyst and the pollutant. The results of the study to determine the percentage of P4R dye degradation are shown in Fig. 6. Experimental findings showed that changes in pH increase the efficiency of the process. In acidic solutions, the positive charge (H^+) on the catalyst surface increases with decreasing pH and activates the catalyst surface. As a result, negative contaminant charges tend to be more adsorbed on the catalyst surface, and the adsorption rate and dye degradation are increased. However, with increasing pH, the presence of a negative charge (^-OH) on

Fig. 5 The rate of percentage of degradation of P4R at different catalyst dosages (0, 0.05, 0.10, 0.15, and 0.20 g). Experimental conditions: concentration of 20 mg L^{-1} of P4R, 0.50 mL H_2O_2, under UV light irradiation and pH
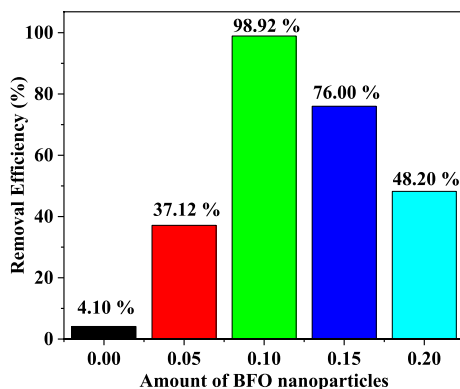
the catalyst increases and causes repulsion between the catalyst and the pollutant, and the amount of degradation decreases. P4R dye degradation in the presence of an acidic environment and a catalyst is very significant [57–59]. Therefore, at pH 2, the maximum amount of P4R dye degradation is observed. Degradation does not occur at natural pH and alkaline pH.

Kinetic study

The photodegradation kinetics of P4R in the presence of $Bi_{1-x}Dy_xFeO_3$ nanoparticles were investigated using the Langmuir–Hinshelwood model by determining the pseudo-first-order rate constant for the photodegradation (Tables 2 and 3). For this purpose, the pseudo-first-order rate constant for photodegradation of P4R was determined based on the nonlinear (Eq. 5) [60–63]:

$$A = x \times e^{-kt} + E \tag{5}$$

The units of the rate constant (k) of pseudo-order unit (min^{-1}), X is the amplitude of the process, and E is the endpoint, both of them have the same units as the measured quantity A. The photodegradation rate constant (k) for a period of 90 min in the presence of the $Bi_{1-x}Dy_xFeO_3$ were 0.01031, 0.02312, 0.01830, and 0.01346 Cm^{-1} for x = 0.00, 0.02, 0.04, and 0.06. P4R degradation percentages of 94.67, 87.69, and 79.69 for x = 0.02, 0.04, and 0.06 in $Bi_{1-x}Dy_xFeO_3$ nanoparticles were obtained for 90 min under the optimal conditions shown in (Fig. 7) instead of 98.92 for 240 min in undoped BFO. Photocatalytic kinetics curve of the Dy-doped BFO (Dy 0.00, 0.02, 0.04, 0.06) nanoparticles it is shown in Fig. S5. The results showed that the rate of the P4R degradation reaction increases significantly with the Dy dopants in the BFO lattice structure.

Table 2 Kinetic study of photodegradation and the percentage of P4R degradation with BFO nanoparticle in 240 min in different conditions

pH value	Amount of BFO (g)	Amount of H2O2 (mL)	Light irradiation conditions	Percentage of degradation of P4R (%)	K1 ± S	X ± S	E ± S	Sum of squared deviations	R2
2	0.10	0.50	UV light	98.92	0.01015 ± 0.001	0.76543 ± 0.032	− 0.093 ± 0.035	0.014284	0.981
4	0.10	0.50	UV light	40.63	0.00721 ± 0.0003	0.32004 ± 0.007	0.324 ± 0.008	0.000233	0.997
6	0.10	0.50	UV light	24.63	0.00051 ± 0.0002	1.36354 ± 0.721	− 0.720 ± 0.721	0.000053	0.998
8	0.10	0.50	UV light	13.62	0.00086 ± 0.0002	0.46232 ± 0.114	0.180 ± 0.115	0.000010	0.999
10	0.10	0.50	UV light	9.32	0.00029 ± 0.0008	0.88255 ± 2.422	− 0.237 ± 2.423	0.000062	0.989
2	0	0.50	UV light	4.10	0.00021 ± 0.0006	0.50943 ± 1.547	0.132 ± 1.547	0.000007	0.992
2	0.05	0.50	UV light	37.12	0.00844 ± 0.0004	0.28723 ± 0.005	0.359 ± 0.006	0.000244	0.997
2	0.15	0.50	UV light	76.00	0.01003 ± 0.0006	0.54467 ± 0.012	0.108 ± 0.013	0.001881	0.994
2	0.20	0.50	UV light	48.20	0.00347 ± 0.0006	0.53503 ± 0.068	0.095 ± 0.071	0.001064	0.992
2	0.10	0	UV light	2.09	0.00041 ± 0.0008	0.14986 ± 0.277	0.492 ± 0.277	0.000003	0.989
2	0.10	0.25	UV light	32.12	0.00040 ± 0.0005	2.11121 ± 2.525	− 1.468 ± 2.527	0.000256	0.995
2	0.10	0.75	UV light	75.21	0.00659 ± 0.0015	0.52653 ± 0.054	0.083 ± 0.061	0.009280	0.967
2	0.10	1	UV light	65.91	0.00666 ± 0.0003	0.58291 ± 0.011	0.124 ± 0.013	0.000440	0.998
2	0.10	0.50	Sunlight	29.64	0.00032 ± 0.0007	2.5081 ± 5.217	− 1.853 ± 5.220	0.000452	0.992
2	0.10	0.50	Dark state	10.31	0.00020 ± 0.0007	1.4535 ± 5.132	− 0.806 ± 5.133	0.000062	0.991

Table 3 Kinetic study and the duration of the P4R degradation process in the presence of 0.10 g $Bi_{1-x}Dy_xFeO_3$ (x = 0, 0.00, 0, 0.02, 0.04 and 0.06) nanoparticles under optimal condition

Nanoparticles	Time (min)	Percentage of degradation of P4R (%)	$K_1 \pm S$	$X \pm S$	$E \pm S$	Sum of squared deviations	R^2
BFO	90	58.46	0.01031 ± 0.002	0.653 ± 0.1009	-0.002 ± 0.105	0.00063	0.994
$Bi_{0.98}Dy_{0.02}FeO_3$	90	94.67	0.02312 ± 0.003	0.782 ± 0.049	-0.083 ± 0.052	0.00313	0.991
$Bi_{0.96}Dy_{0.04}FeO_3$	90	87.69	0.01830 ± 0.002	0.764 ± 0.047	-0.079 ± 0.052	0.00133	0.995
$Bi_{0.94}Dy_{0.06}FeO_3$	90	79.69	0.01346 ± 0.004	0.806 ± 0.158	-0.109 ± 0.169	0.00452	0.982

Fig. 7 The rate of percentage of P4R photocatalytic degradation using Dy-doped BFO nanoparticles with values of 0.02, 0.04, and 0.06. Experimental conditions: concentration of 20 mg L^{-1} of P4R, 0.50 mL H_2O_2, 0.10 g of the Dy-doped BFO nanoparticles, under UV light irradiation and pH 2
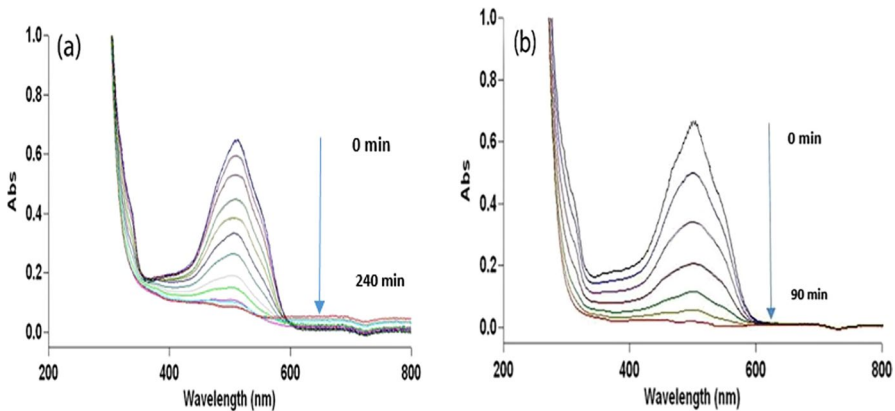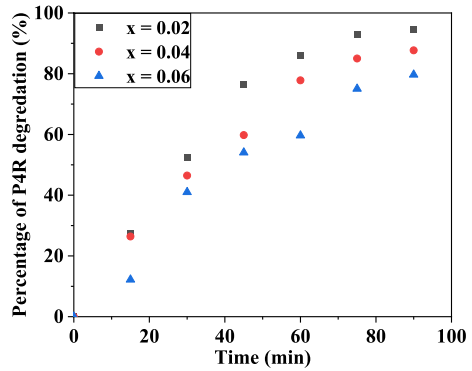
Fig. 8 UV–Vis absorption spectra of the P4R dye degradation process under experimental conditions: concentration of 20 mg L^{-1} of P4R, 0.50 mL H_2O_2, 0.10 g of the Dy-doped BFO nanoparticles, under UV light irradiation and pH 2 at $\lambda_{max} = 508$ nm in the presence of **a** un-doped BFO in 240 min and **b** Dy-doped BFO (Dy 2%) in 90 min

Conclusion

Two photocatalysts, including BFO and Dy-doped BFO with different values of Dy 0.02, 0.04, and 0.06, were synthesized using a chemical method for P4R degradation under UV light exposure. The morphology and structure of the photocatalysts were evaluated using various techniques to investigate the success of their preparation. Different factors, such as irradiation type, H_2O_2 values, photocatalyst amount, and pH, were selected as influential factors in the photodegradation of P4R. These factors were optimized for each photocatalyst to obtain the best degradation conditions. Under optimum degradation conditions, the percentages of P4R degradation for each photocatalyst were studied, indicating the percentages of P4R degradation using BFO for 240 min 98.92%, using BFO Dy-doped (Dy 2%), (Dy 4%) and (Dy 6%) for 90 min 94.67%, 87.69% and 79.69% (Fig. 8). Besides, the Langmuir–Hinshelwood model kinetics were selected to evaluate and determine the rate constant of the photodegradation procedure in the presence of BFO and Dy-doped BFO. The rate constants showed that the highest P4R degradation rate was displayed using Dy-doped BFO (Dy 2%). In other words, the P4R degradation rate was significantly increased by increasing Dy (III) ions as a dopant in the BFO lattice through forming trapping sites in the BFO structure as suitable electron acceptor species and improving the stability of electron–hole pairs and lives. Also, the pore size of the BFO nanoparticles decreases with an increasing percentage of dysprosium doped into the BFO structure, leading to an increase in selectivity for the penetration of present molecules in the sample solution, such as contaminants into the BFO lattice. An essential advantage of BFO and Dy-BFO is their single-step and straightforward synthesis, which accelerates the synthesis of photocatalyst.

References

1. Ghimpusan M, Nechifor G, Nechifor A-C, Dima S-O, Passeri P (2017) Case studies on the physical-chemical parameters' variation during three different purification approaches destined to treat wastewaters from food industry. J Environ Manag 203:811–816
2. Natarajan S, Bajaj HC, Tayade RJ (2018) Recent advances based on the synergetic effect of adsorption for removal of dyes from waste water using photocatalytic process. J Environ Sci 65:201–222
3. El-Nemr A (2012) Non-Conventional textile waste water treatment. Nova Science Publishers, New York
4. Al-Nuaim MA, Alwasiti AA, Shnain ZY (2023) The photocatalytic process in the treatment of polluted water. Chem Zvesti 77:677–701
5. Yang H, Zhu M, Li Y (2023) Sol–gel research in China: a brief history and recent research trends in synthesis of sol–gel derived materials and their applications. J Solgel Sci Technol 106:406–421
6. Shahbazi M-A, Faghfouri L, Ferreira MP, Figueiredo P, Maleki H, Sefat F, Hirvonen J, Santos HA (2020) The versatile biomedical applications of bismuth-based nanoparticles and composites: therapeutic, diagnostic, biosensing, and regenerative properties. Chem Soc Rev 49:1253–1321
7. Mukherjee A, Basu S, Green L, Thanh N, Pal M (2015) Enhanced multiferroic properties of Y and Mn codoped multiferroic $BiFeO_3$ nanoparticles. J Mater Sci 50:1891–1900

8. Li B, Wang C, Liu W, Ye M, Wang N (2013) Multiferroic properties of La and Mn co-doped $BiFeO_3$ nanofibers by sol–gel and electrospinning technique. Mater Lett 90:45–48

9. Rabbani M, Rahimi R, Farajnejad Ghadi H (2018) Photocatalytic application of $BiFeO_3$ synthesized via a facile microwave-assisted solution combustion method. J Solgel Sci Technol 87:340–346

10. Di L, Yang H, Xian T, Chen X (2017) Enhanced photocatalytic activity of $NaBH_4$ reduced $BiFeO_3$ nanoparticles for rhodamine B decolorization. Materials 10:1118

11. Basith M, Yesmin N, Hossain R (2018) Low temperature synthesis of $BiFeO_3$ nanoparticles with enhanced magnetization and promising photocatalytic performance in dye degradation and hydrogen evolution. RSC Adv 8:29613–29627

12. Lam S-M, Sin J-C, Mohamed AR (2017) A newly emerging visible light-responsive $BiFeO_3$ perovskite for photocatalytic applications: a mini review. Mater Res Bull 90:15–30

13. Guo Y, Pu Y, Cui Y, Hui C, Wan J, Cui C (2017) A simple method using citric acid as the template agent to improve photocatalytic performance of $BiFeO_3$ nanoparticles. Mater Lett 196:57–60

14. Bharathkumar S, Sakar M, Balakumar S (2016) Experimental evidence for the carrier transportation enhanced visible light driven photocatalytic process in bismuth ferrite ($BiFeO_3$) one-dimensional fiber nanostructures. J Phys Chem C 120:18811–18821

15. Wang X, Mao W, Zhang Q, Wang Q, Zhu Y, Zhang J, Yang T, Yang J, Li XA, Huang W (2016) PVP assisted hydrothermal fabrication and morphology-controllable fabrication of $BiFeO_3$ uniform nanostructures with enhanced photocatalytic activities. J Alloys Compd 677:288–293

16. Bharathkumar S, Sakar M, Balakumar S (2015) Versatility of electrospinning in the fabrication of fibrous mat and mesh nanostructures of bismuth ferrite ($BiFeO_3$) and their magnetic and photocatalytic activities. Phys Chem Chem Phys 17:17745–17754

17. Kundys B, Viret M, Colson D, Kundys DO (2010) Light-induced size changes in $BiFeO_3$ crystals. Nat Mater 9:803–805

18. Sakar M, Balakumar S, Saravanan P, Bharathkumar S (2015) Compliments of confinements: substitution and dimension induced magnetic origin and band-bending mediated photocatalytic enhancements in $Bi_{1-x}Dy_xFeO_3$ particulate and fiber nanostructures. Nanoscale 7:10667–10679

19. Sakar M, Balakumar S, Saravanan P, Jaisankar S (2013) Annealing temperature mediated physical properties of bismuth ferrite ($BiFeO_3$) nanostructures synthesized by a novel wet chemical method. Mater Res Bull 48:2878–2885

20. Chakrabarti K, Sarkar B, Ashok VD, Das K, Chaudhuri SS, De S (2013) Interfacial magnetism and exchange coupling in $BiFeO_3$–CuO nanocomposite. Nanotechnol 24:505711

21. Gao F, Chen X, Yin K, Dong S, Ren Z, Yuan F, Yu T, Zou Z, Liu JM (2007) Visible-light photocatalytic properties of weak magnetic $BiFeO_3$ nanoparticles. Adv Mater 19:2889–2892

22. Ji W, Yao K, Lim Y-F, Liang YC, Suwardi A (2013) Epitaxial ferroelectric $BiFeO_3$ thin films for unassisted photocatalytic water splitting. Appl Phys Lett 103:062901

23. Uniyal P, Yadav K (2009) Fast track communication: observation of the room temperature magnetoelectric effect in Dy doped $BiFeO_3$. J Phys Condens Matter 21:012205

24. Khataee A, Darvishi Cheshmeh Soltani R, Hanifehpour Y, Safarpour M, Gholipour Ranjbar H, Joo SW (2014) Synthesis and characterization of dysprosium-doped ZnO nanoparticles for photocatalysis of a textile dye under visible light irradiation. Ind Eng Chem Res 53:1924–1932

25. Banoth P, Sohan A, Kandula C, Kollu P (2022) Structural, dielectric, magnetic, and ferroelectric properties of bismuth ferrite ($BiFeO_3$) synthesized by a solvothermal process using hexamethylenetetramine (HMTA) as precipitating agent. Ceram Int 48:32817–32826

26. Singh S, Yadawa Y, Ranjan A (2023) Enhanced adsorption of methylene blue by mixed-phase bismuth ferrite prepared by non-aqueous sol-gel route. J Environ Chem Eng 11:109229

27. Sun H, Sun N, Li H, Zhang J, Yang Y (2013) Development of multiresidue analysis for 21 synthetic colorants in meat by microwave-assisted extraction–solid-phase extraction–reversed-phase ultrahigh performance liquid chromatography. Food Anal Methods 6:1291–1299

28. Tanaka T (2006) Reproductive and neurobehavioural toxicity study of tartrazine administered to mice in the diet. Food Chem Toxicol 44:179–187

29. EFSA Panel on Food Additives and Nutrient Sources Added to Food (2009) Scientific opinion on the re-evaluation of Ponceau 4R (E 124) as a food additive. EFSA J 7:1328

30. Sati PC, Kumar M, Chhoker S (2015) Low temperature ferromagnetic ordering and dielectric properties of $Bi_{1-x}Dy_xFeO_3$ ceramics. Ceram Int 41:3227–3236

31. Muneeswaran M, Giridharan N (2014) Effect of Dy-substitution on the structural, vibrational, and multiferroic properties of $BiFeO_3$ nanoparticles. J Appl Phys 115:214109

32. Macías-Quiroga IF, Rojas-Méndez EF, Giraldo-Gómez GI, Sanabria-González NR (2020) Experimental data of a catalytic decolorization of Ponceau 4R dye using the cobalt (II)/$NaHCO_3$/H_2O_2 system in aqueous solution. Data Brief 30:105463

33. Shabbir A, Gilani Z, Nawaz A, Warsi M, Khan M (2016) Enhanced dielectric and photocatalytic behaviour of Dy-Co co-doped multiferroic $BiFeO_3$ nanoparticles. Dig J Nanomater Bios 11:1189–1195

34. Shannon RD (1976) Revised effective ionic radii and systematic studies of interatomic distances in halides and chalcogenides. Acta Crystallogr A Cryst Phys Diffr Theor Gen Crystallogr 32:751–767

35. Arora M, Sati PC, Chauhan S, Singh H, Yadav K, Chhoker S, Kumar M (2013) Structural, magnetic and optical properties of $Bi_{1−x}Dy_xFeO_3$ nanoparticles synthesized by sol–gel method. Mater Lett 96:71–73

36. Khoshnood RS, Khoshnoud DS (2019) Structural, magnetic, and photocatalytic properties in $Bi_{0.83−x}La_{0.17}Y_xFeO_3$ nanoparticles. Appl Phys A 125:1–10

37. Nakhaei M, Khoshnoud DS (2019) Influence of particle size and lattice distortion on magnetic and dielectric properties of $NdFeO_3$ orthoferrite. Physica B Condens Matter 553:53–58

38. Rahimkhani M, Khoshnoud DS, Ehsani M (2018) Origin of enhanced multiferroic properties in $Bi_{0.85−x}La_{0.15}Ho_xFeO_3$ nanopowders. J Magn Magn Mater 449:538–544

39. Carranza-Celis D, Cardona-Rodríguez A, Narváez J, Moscoso-Londono O, Muraca D, Knobel M, Ornelas-Soto N, Reiber A, Ramírez JG (2019) Control of multiferroic properties in $BiFeO_3$ nanoparticles. Sci Rep 9:3182

40. Saghafi A, Sanavi Khoshnood R, Sanavi Khoshnoud D, Eshaghi Z (2022) Preconcentration and determination of four antibiotics in biological samples using nanofluid-assisted magnetic dispersive micro-solid-phase extraction coupled with high-performance liquid chromatography. Chem Zvesti. https://doi.org/10.1007/s11696-021-01903-5

41. Ayoub M, Morad I, Ali HE, Mostafa M, El–Desoky M (2021) Influence of BaO doping on the structural, ac conductivity, and dielectric properties of $BiFeO_3$ multiferroic nanoparticles. J Inorg Organomet Polym Mater. https://doi.org/10.21203/rs.3.rs-204688/v1

42. Mumtaz F, Nasir S, Jaffari GH, Shah SI (2021) Chemical pressure exerted by rare earth substitution in $BiFeO_3$: effect on crystal symmetry, band structure and magnetism. J Alloys Compd 876:160178

43. Ahmad SI (2022) Nano cobalt ferrites: doping, structural, low-temperature, and room temperature magnetic and dielectric properties—a comprehensive review. J Magn Magn Mater. https://doi.org/10.1016/j.jmmm.2022.169840

44. Varak Neshin M, Sanavi Khoshnood R, Sanavi Khoshnoud D (2022) Surfactant assisted magnetic dispersive micro solid phase extraction-HPLC as a straightforward and green procedure for preconcentrating and determining caffeine, lidocaine, and chlorpromazine in biological and water samples. J Environ Anal Chem. https://doi.org/10.1080/03067319.2021.2014473

45. Saghafi A, Khoshnood RS, Khoshnoud DS, Es'Haghi Z (2022) Magnetic properties and photocatalytic activity of Bi1-xSmxFe1-yNiyO3 nanoparticles for methyl red degradation. Reac Kinet Mech Cat 135:3375–3391

46. Xian T, Yang H, Dai J, Wei Z, Ma J, Feng W (2011) Photocatalytic properties of $BiFeO_3$ nanoparticles with different sizes. Mater Lett 65:1573–1575

47. Hao C, Xiang J, Hou H, Lv W, Lv Y, Hu W, Liu Z (2014) Photocatalytic performances of $BiFeO_3$ particles with the average size in nanometer, submicrometer, and micrometer. Mater Res Bull 50:369–373

48. Hu Z, Chen D, Wang S, Zhang N, Qin L, Huang Y (2017) Facile synthesis of Sm-doped $BiFeO_3$ nanoparticles for enhanced visible light photocatalytic performance. Mater Sci Eng 220:1–12

49. Dhanalakshmi R, Muneeswaran M, Shalini K, Giridharan N (2016) Enhanced photocatalytic activity of La-substituted $BiFeO_3$ nanostructures on the degradation of phenol red. Mater Lett 165:205–209

50. Fatima S, Ali SI, Iqbal MZ, Rizwan S (2020) Congo red dye degradation by graphene nanoplatelets/doped bismuth ferrite nanoparticle hybrid catalysts under dark and light conditions. J Catal 10:367

51. Irfan S, Zhuanghao Z, Li F, Chen Y-X, Liang G-X, Luo J-T, Ping F (2019) Critical review: bismuth ferrite as an emerging visible light active nanostructured photocatalyst. J Mater Res Technol 8:6375–6389

52. Abd El-Raady AA, Nakajima T (2006) Effect of UV radiation on the removal of carboxylic acids from water by H_2O_2 and O_3 in the presence of metallic ions. Ozone Sci Eng 28:53–58

53. Neshin MV, Khoshnood RS, Khoshnoud DS (2021) Enhanced photocatalytic activity of Ni-doped $BiFeO_3$ nanoparticles for degradation of bromophenol blue in aqueous solutions. Reac Kinet Mech Cat 134:951–970

54. Tayeb AM, Hussein DS (2015) Synthesis of TiO_2 nanoparticles and their photocatalytic activity for methylene blue. J Nanomater 3:57–63

55. Li Y, Zheng X, Yang J, Zhao Z, Cui S (2021) Enhanced photocatalytic degradation of 2, 4, 6-trichlorophenol and RhB with RhB-sensitized BiOClBr catalyst based on response surface methodology. J Taiwan Inst Chem Eng 119:213–223

56. Vijay S, Balakrishnan RM, Rene ER, Priyanka U (2019) Photocatalytic degradation of irgalite violet dye using nickel ferrite nanoparticles. J Water Supply: Res Technol AQUA 68:666–674

57. Mousavi S, Shahraki F, Aliabadi M, Haji A, Deuber F, Adlhart C (2019) Nanofiber immobilized CeO_2/dendrimer nanoparticles: an efficient photocatalyst in the visible and the UV. Appl Surf Sci 479:608–618

58. Ariza-Tarazona MC, Villarreal-Chiu JF, Hernández-López JM, De la Rosa JR, Barbieri V, Siligardi C, Cedillo-González EI (2020) Microplastic pollution reduction by a carbon and nitrogen-doped TiO_2: effect of pH and temperature in the photocatalytic degradation process. J Hazard Mater 395:122632

59. Alkaim A, Aljeboree A, Alrazaq N, Baqir S, Hussein F, Lilo A (2014) Effect of pH on adsorption and photocatalytic degradation efficiency of different catalysts on removal of methylene blue. Asian J Chem 26:8445

60. Lente G (2018) Facts and alternative facts in chemical kinetics: remarks about the kinetic use of activities, termolecular processes, and linearization techniques. Curr Opin Chem Eng 21:76–83

61. Lente G (2015) Deterministic kinetics in chemistry and systems biology: the dynamics of complex reaction networks. Springer, Cham

62. Roguai S, Djelloul A (2022) Elaboration, characterization and applications of SnO_2, 2% Gd-SnO_2 and 2% Gd-9% F-SnO_2 thin films for the photocatalytic degradation of MB by USP method. Inorg Chem Commun 138:109308

63. Roguai S, Djelloul A (2021) A simple synthesis of CuO NPs for photocatalytic applications and theirs structural and optical properties. JNTM 11:53–57

Authors and Affiliations

Elaheh Mahmoudi Doroh[1] · Razieh Sanavi Khoshnood[1] 🟢 **·
Davoud Sanavi Khoshnoud[2] · Zarrin Es′haghi[1,3]**

✉ Razieh Sanavi Khoshnood
　rskhoshnood@yahoo.com

　Elaheh Mahmoudi Doroh
　mahmoodi_elahe67@yahoo.com

　Davoud Sanavi Khoshnoud
　dskhoshnoud@semnan.ac.ir

　Zarrin Es′haghi
　zeshaghi@pnu.ac.ir

[1]　Department of Chemistry, Mashhad Branch, Islamic Azad University, Mashhad, Iran

[2]　Faculty of Physics, Semnan University, P. O. Box 35195-363, Semnan, Iran

[3]　Department of Chemistry, Payame Noor University, Tehran, Iran